

Electrostatic force microscopy analysis of $\text{Bi}_{0.7}\text{Dy}_{0.3}\text{FeO}_3$ thin films prepared by pulsed laser deposition integrated with ZnO films for microelectromechanical systems and memory applications

Deepak Bhatia³, Sandipta Roy², S. Nawaz², R.S. Meena³, V.R. Palkar¹

¹ Department of Electrical Engineering and Centre for Excellence in Nanoelectronics, Indian Institute of Technology Bombay, Mumbai-400076, India

² Centre for Research in Nanotechnology and Science, Indian Institute of Technology Bombay, Mumbai-400076, India

³ Department of Electronics Engineering, Rajasthan Technical University, Kota-324010, India

Corresponding author: Deepak Bhatia (dbhatia@rtu.ac.in)

Received 27 February 2017 ♦ Accepted 12 March 2018 ♦ Published 1 June 2018

Citation: Bhatia D, Roy S, Nawaz S, Meena RS, Palkar VR (2018) Electrostatic force microscopy analysis of $\text{Bi}_{0.7}\text{Dy}_{0.3}\text{FeO}_3$ thin films prepared by pulsed laser deposition integrated with ZnO films for microelectromechanical systems and memory applications. *Modern Electronic Materials* 4(2): 77–85. <https://doi.org/10.3897/j.moem.4.2.33306>

Abstract

In this paper, we report the charge trapping phenomena in zinc oxide (*n*-ZnO) and $\text{Bi}_{0.7}\text{Dy}_{0.3}\text{FeO}_3$ (BDFO)/ZnO thin films deposited on *p*-type <100> conducting Si substrate. The significant change in contrast above the protrusions of ZnO verifies the possibility of heavy accumulation of injected holes in there. The ZnO and BDFO/ZnO films were characterized by the electrostatic force microscopy (EFM) to understand the phase dependence phenomenon on the bias supporting electron tunnelling. The EFM has an important role in the analysis of electrical transport mechanism characterization and electric charge distribution of local surface in nanoscale devices. It was observed that in BDFO/ZnO, the contrast of EFM images remains constant with the bias switching and that primarily indicates availability of trap sites to host electrons. The change in contrast over the protrusions of ZnO suggests that mobility of the electrical charge carriers may be through the grain boundary. The formation of these hole-trapped sites may be assumed by bond breaking phenomenon.

Keywords

BDFO/ZnO, EFM, multiferroics

1. Introduction

To study the charge trapping phenomena in semiconductor zinc oxide and combination of magnetoelectric multiferroic $\text{Bi}_{0.7}\text{Dy}_{0.3}\text{FeO}_3$ (BDFO)/ZnO thin films deposited

on *p*-type Si substrate is an interesting subject. The excellent multifunctional properties of BDFO/ZnO films may be advantageous for a variety of device applications like sensors, energy scavengers, electricity generators, etc [1]. The appeal of combining of piezoelectric with multifer-

roics offers great possibility of the storage of generated energy through vibrations with best qualities of ferroelectric random-access memory (**FeRAMs**) and magnetoresistive RAM (**MRAMs**) with fast low-power electrical write operation.

Zinc oxide (**ZnO**) is a major contributor in the research field of oxide electronics and may be defined as a future material of choice. This material is suitable for fabrication of the optoelectronic [2], piezoelectric [3] and spintronics devices [4]. Nano-crystalline thin films of ZnO have already been popular for photovoltaic device applications as transparent conductive oxide (**TCO**) owing to its inherent transparency property [5–8] in the visible range [9–10]. Also *n*-doped ZnO may be used as the buffer layer for blocking of electron collector/hole in inverted bulk-heterojunction organic solar cells [11–12] and in fast scalable memories [1].

The interface between electrode and ferroelectric layer gives rise to complex interfacial physics leads towards degradation of performance of ferroelectric memory elements. The applications of multiferroics are that, they offer the feasibility of best qualities of memory devices with fast low-power electrical write operation, and non-destructive magnetic read operation in a single combination [13–17]. Magnetoelectric multiferroic modified BiFeO₃ (Bi_{0.7}Dy_{0.3}FeO₃ or BDFO) is promising ferroelectric material, exhibiting the ideal properties at room temperature. The BDFO film has unique multifunctional properties such as low leakage, low interface state density and very high dielectric constant ($k > 30$), and may provide the storage of generated electricity [18–19]. Here we report the results of a study on the charge trapping mechanism in the Au/BDFO/ZnO/Si metal–insulator–semiconductor (**MIS**) interfaces for different bias voltages. The trapping behaviour of the charge carriers in thin *n*-type ZnO/*p*-Si semiconductor heterojunction diode was also studied.

1.1 Theory

EFM is used mainly to characterize materials for electrical properties. During the measurements, the tip of standard non-contact EFM system carries out a main scan and an interleave scan on each scanning line. The main scan performs the recording of the surface topographical data in an intermittent contact (tapping) mode [20]. In the consecutive interleave scan mode the AFM tip is raised above the sample surface (whose topography was acquired in the main scan) and is kept at a fixed height during the scan. In the interleave scan duration, the biasing with respect to the sample is provided to the tip and it observes an electrostatic force at a distance S from the sample surface is given by [21]:

$$F(s) = \frac{1}{2} \frac{dC}{dS} (\Delta V)^2. \quad (1)$$

Where ΔV is the potential difference and C is the value of capacitance between the sample and the probe. In the

contrast method of EFM-phase measurements technique, the tip is driven mechanically and oscillations are made during the interleave scan. The resonant frequency and phase shift of the tip due to the electrostatic force gradient dF/dS are observed. The resonant frequency (ω) and phase shift (ϕ) may be defined by the equations 2 and 3 for the small force gradients [21].

$$\Delta\omega = -\frac{\omega_0}{2k_e} \frac{dF}{dS} \quad (2)$$

and

$$\Delta\phi = -\arcsin\left(\frac{Q}{k_e} \frac{dF}{dS}\right), \quad (3)$$

where cantilever's quality factor is « Q » and « k_e » is the spring constant. The additional description, practical information and applications of EFM are available in detail and discussed elsewhere [22–23]. In extension to conventional topography image, the EFM measurement technique records the phase shift in parallel. Since

$$\frac{dF(s)}{dS} = \frac{1}{2} \frac{d^2C}{dS^2} (\Delta V)^2. \quad (4)$$

Then we have

$$\Delta\phi = -\arcsin\left(\frac{Q}{2k_e} \frac{d^2C}{dS^2} (\Delta V)^2\right). \quad (5)$$

It is noticed from the equations (4) and (5), the phase and frequency shift is governed by the potential difference ΔV between the tip and the sample surface and finally lateral distribution of d^2C/dS^2 determines the resolution of the EFM-phase method. This phase shift is always observed to be negative due to the positive value of d^2C/dS^2 . At the same time, owing to the fact that dC/dS is negative the electrostatic forces between the tip and sample surface are attractive.

EFM is also used for mapping of the vertical gradient (S) of the electric field between the sample surface and the tip against the in-plane (X, Y) coordinates. The trapped charges create a field on or below the surface of sample are often adequately large to form a good contrast in an EFM image [24]. The electrical force gradient (dF/dS) of the cantilever, experienced by the tip can be related with phase shift mapping $\Delta\phi$ by the equation given by equation 6 [21]

$$\tan(\Delta\phi) \approx \frac{k_e}{Q} \frac{dF}{dS}. \quad (6)$$

Where Q is quality factor and k_e is elastic constant of the cantilever [24]. The fundamental model for tip-sample arrangement has been developed for quantitative analysis. The trapped charged centre is assumed to be at a position which is located at the ZnO surface or the BDFO/ZnO interface as shown in Fig. 1. Because of its relatively short retention time the trapped charges in the BDFO are assumed to be ignorable [25–26].

The exerted forces F is the combination of the capacitive and the coulomb force. The trapped charge, q_{trap} cre-

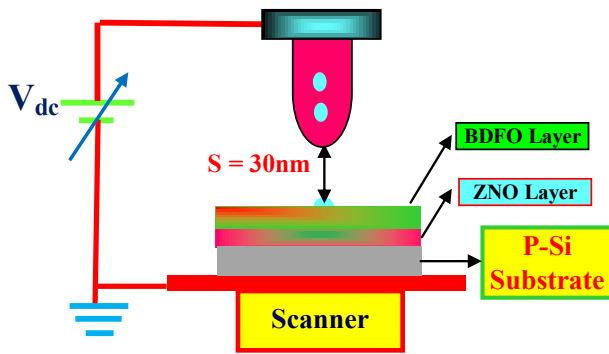


Figure 1. Experimental setup for sample and EFM structure.

ates the image charges (q_i) at the tip and as well as in the semiconductor, where $|-q'_{\text{trap}}| = 2q_{\text{trap}}/(1 + \epsilon_{\text{sc}})$. Where ϵ_{sc} is the dielectric constant of ZnO layer. The amount of total tip charge is equal to the sum of the tip bias charge q_{dc} and $-q'_{\text{trap}}$. The surface of tip may be conducted as a sphere-plate capacitor [22] at a distance of 25–45 nm [22–23]. So, the exerted force F is defined as follows [27]

$$F \approx \frac{-q'_{\text{trap}}{}^2}{4\pi\epsilon_0 [2(s+t_d)]^2} + \frac{q'_{\text{trap}}CV_{\text{dc}}}{4\pi\epsilon_0 [2(s+R_{\text{tip}}+t_d)]^2} + \frac{1}{2} \frac{\partial C}{\partial S} V_{\text{dc}}^2. \quad (7)$$

Where R_{tip} is the tip radius and t_d is the distance between centre of the charge to the sample surface. More expanded terms with q_i are excluded for simplicity. Due to the presence of Coulomb force acting between the embedded charge and the image charge, the first term is introduced in the equation (7). Appearance of the second term is from Coulomb forces between the embedded charge and the bias of EFM tip [24, 25]. The third term defines the capacitive force among the sample and the EFM tip. If the EFM images are acquired at different applied voltages, the actual contribution of the every term can be evaluated in the total force gradient F . Initially tip of the EFM was fixed at a certain point on the sample and tip bias was changed gradually in small steps from -5 V to $+5$ V. The EFM phase versus tip bias having a parabolic relationship (1) indicates that the capacitive forces are essentially loaded onto the EFM tip (2) and the brightness of EFM image also enhanced with movement of phase more toward in the negative direction because there is a additional attractive force between tip and sample. It is also possible to calculate the approximate capacitance from the curvature. This effect of capacitance may be removed by applying the voltage of the identical amplitude in turn but in opposite sign and the difference is compared.

2. Experimental Details

A ZnO (99.9%) target of diameter 2 inch was used to deposit ZnO film of 300 nm thickness on RCA (standard Radio Corporation of America) cleaned [9] p -type conducting (0.0001–0.0005 ohm-cm) Si $\langle 100 \rangle$ substrates by dielectric sputtering process. The deposition process was carried out in Ar environment with a RF power of 100W.

The base pressure was 5×10^{-5} mbar and operating pressure was maintained at $2.2 \cdot 10^{-2}$ mbar during deposition. Pulsed laser deposition technique (PLD) was used to deposit BDFO film of 300 nm thickness on ZnO/Si with a Complex Pro 201,248 nm KrF excimer laser from Coherent. The deposition parameters are: laser density – 2 J/cm^2 , distance between target to substrate – 5 cm, substrate temperature – $650 \text{ }^\circ\text{C}$, O_2 Pressure – $4.5 \cdot 10^{-1}$ mbar, Repetition Rate = 10 Hz and No. of Pulses – 22500 [1].

Various techniques were employed for characterization of BDFO/Zno/Si films. The thicknesses of the films were measured by profilometer (Dektak XT). X-ray diffraction (Rigaku, Cu- K_α radiation, $\lambda = 1.5405 \text{ \AA}$) was used to determine the phase purity and crystal structure of the film. A Multimode Scanning Probe Microscope (Veeco Digital Instruments make Nanoscope IV) was used to carry out the electric force microscopy of the samples. It was equipped with an optical microscope for area selection. It can zoom-in to examine details up to the limit of the tip's resolution and high phase sensitivity. Digital image processing and analysis software (Nanoscope 6.2r1) was used to analyze the raw data. The energy-band diagram of the device is shown in Fig. 2.

The electron affinities of ZnO and Si are used as 4.31

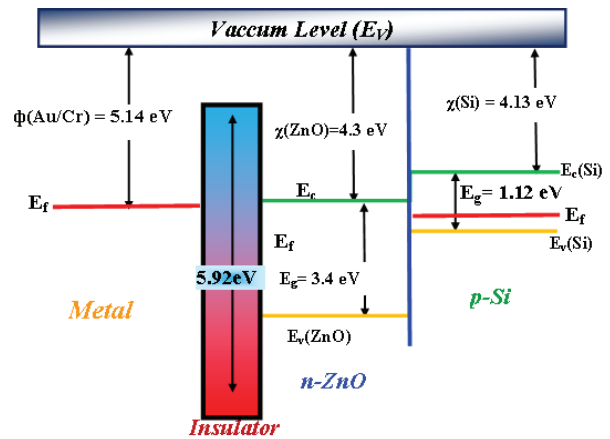


Figure 2. Energy band diagram of Au/Cr/BDFO/ZnO/Si MIS Structure.

and 4.13 eV respectively [28–29], the offsets of conduction-band ($\Delta E_c = \chi_{\text{ZnO}} - \chi_{\text{Si}}$) and valance-band ($\Delta E_v = \Delta E_g + \Delta E_c$) are 0.17 and 2.45 eV obtained for n -ZnO/ p -Si heterojunction. The movement of holes from Si to ZnO is restricted by the large difference between the valence-band offset and conduction-band offset. Thus, the current transport in the device is dominated by the flow of electrons from the n -ZnO to the p -Si [28–31].

3. Results and discussion

XRD Patterns obtained for ZnO and BDFO/ZnO is shown in Fig. 3 (a and b). XRD peaks of BDFO exhibit a perovskite structure similar to that of pure BiFeO_3 (BFO) and belong to R3c space group. Substitution of Dy had affected the structure of parent compound, BFO and enhancement

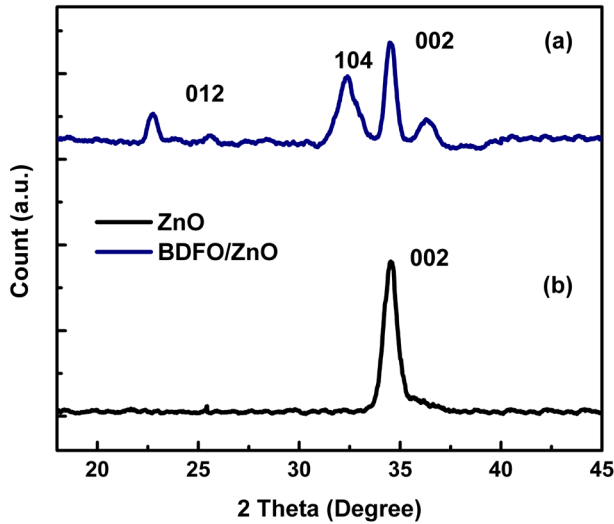


Figure 3. X-ray diffraction pattern obtained for ZnO and BDFO/ZnO thin films grown on Si substrate.

in ferromagnetism ordering was observed [32]. The peak locations of BDFO are at $\sim 20.37^\circ$ and $\sim 31.88^\circ$, and matches with similar experimentations in the reported literature [1, 19, 27]. All the peaks of the patterns were indexed.

The XRD pattern of ZnO film deposited on Si substrate is single phase and polycrystalline in nature [1] as shown in Fig. 3 (b). This could be due to the lattice mismatch between ZnO and Si substrate. It can also be seen from the pattern that diffraction peak located at $\sim 34.396^\circ$ is very sharp. This indicates that the deposited ZnO thin film on the Si substrate has a high c-axis (002) preferred orientation, which is necessary to achieve a ZnO film with high piezoelectric quality [11, 33]. The average value of grain size of the nanoparticles in the BDFO/ZnO and ZnO films has been determined (~ 43 – 49 nm) from XRD peak broadening by using Debye–Scherer relation (eq. 8) [32]

$$D = \frac{0.89\lambda_s}{(\beta - \beta_i)\cos\theta} \quad (8)$$

where λ_s is the wavelength of X-ray Source (1.5405 \AA), β and β_i (arises from the instrument) are the full width at

half maximum (FWHM) of the diffraction peaks and the angle of diffraction is θ .

To determine the grain morphology of BDFO/ZnO and ZnO films, Scanning electron microscopy (SEM) was performed using Raith150Two. It is also used to find the uniformity and the thickness of BDFO films over ZnO films. The SEM images reveal the BDFO coating with granular structure. More details on SEM images are reported in our earlier paper [29]. It indicates that the of BDFO film over ZnO film is polycrystalline in nature. The columnar texture of the BDFO films over ZnO films signifies that the deposited ZnO film has highly c-axis-orientation with hexagonal crystals. It also indicates uniform grain morphology with the grain size of the order of 40–70 nm.

A scanning probe microscope (Nanoscope IV Multimode, Veeco Digital Instruments) was used to obtain non-contact mode AFM [Fig. 4 (a–c)] and EFM images operated under ambient conditions. The root-mean-square (RMS) value of the surface roughness of BDFO/ZnO/Si evaluated by AFM is about 4.25 nm and is comparable to that reported by Yao Wang et. al. [34]. While RMS value of surface roughness is measured as 3.61 nm for the ZnO/Si. All AFM (topographic) and EFM measurements were obtained using a Micromasch conductive Pt–Ti cantilever.

A set of EFM images (a–c) of *n*-type ZnO is shown in Fig. 5, which is sequentially obtained from the 0, +5 V, –5 V bias. The sample scanned area was taken of $500 \times 500 \text{ nm}^2$ and the tip lift-off height was maintained at 30 nm, which is somewhat greater than the roughness of surface. The bright and dark areas correspond to domains with the polarization in the EFM images. It has been observed that there is an image charge reversal occurs (due to columbic forces) by changing the bias from –5V to +5V or +5V to –5V. Brighter part is more positively charged and darker one is more negative. This charge phenomenon can be defined in the following way: For the positive bias more electrons are tunnelled inwards in the area inferior than surroundings and similarly more electrons are tunnelled out for the negative tip bias or sample bias. Thus the surface always exerts an attractive force on the tip and the magnitude of this force is determined by

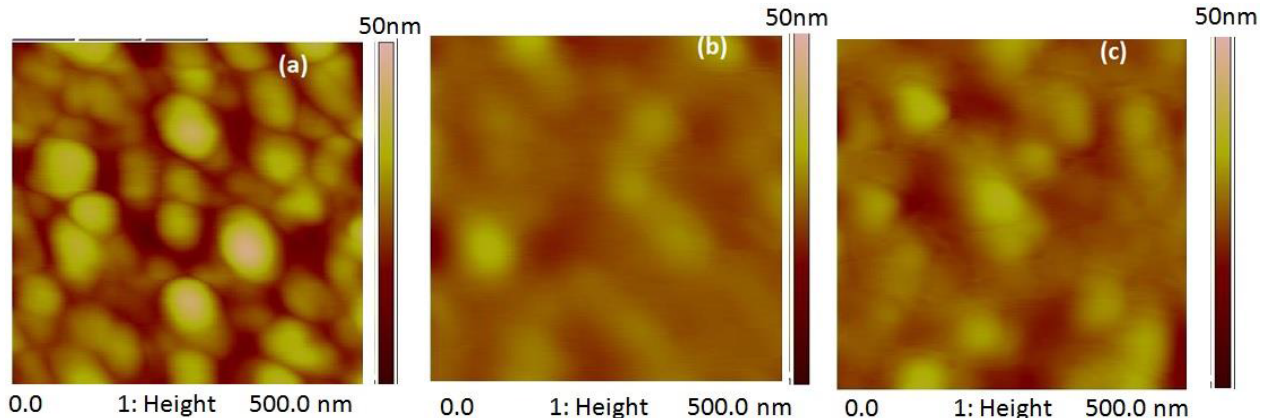


Figure 4. The sets of AFM images (a–c) of *n*-type ZnO thin film on 50 nm color scale. Sample scan area is 500 nm and the tip lift-off height is 30 nm, phase sign is decided negative. The sample biases are 0 V, +5V and –5V respectively.

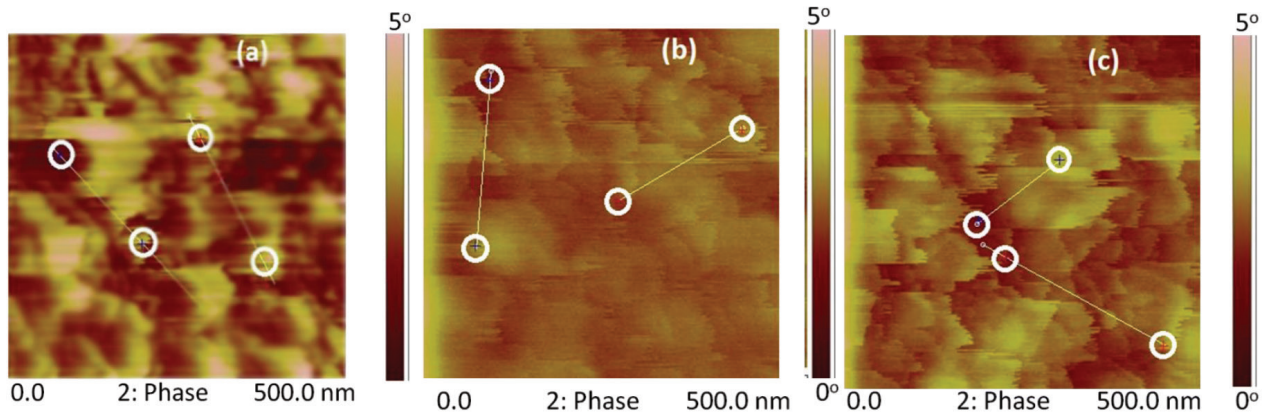


Figure 5. The sets of EFM images for ZnO thin film (a–c) on 5° color scale. Sample Scan area is 500 nm and the tip lift-off height is 30 nm. The sample biases are 0 mV, +5V and –5V respectively.

the electric field whose value is governed by the thickness. When the tip bias is changed from +5 to –5 V the observed average phase difference is about 0.94° in the images observed from Fig. 5 (b and c). Thus the trapped charge (q_{trap}) which is governed by equations (1) and (2) takes the following form:

$$q'_{\text{trap}} = \frac{2\pi\epsilon_0 k_c}{|V_{\text{dc}}| Q} (\tan \Delta\phi_+ - \tan \Delta\phi_-) \left\{ \frac{d}{ds} \left[\frac{C}{(s + R_{\text{tip}} + t_d)^2} \right] \right\}^{-1} \quad (9)$$

The change in phase with positive bias ($+V_{\text{dc}}$) to negative bias ($-V_{\text{dc}}$) is referred as $\Delta\phi$ [2]. In Fig. 6 at the locations shown by the circles, when the tip bias is 0 V the phase contrast is detected. This phase contrast goes bright (attractive) at –5 V and altered to dark (repulsive) at +5 V when the sample-tip bias is switched to +5 V. This contrast inversion occurs, while second term due to Coulomb forces of eq. (7) is greater than the third capacitive term. The EFM phase is dependent to the sample and EFM tip bias. Therefore, it can be said that positive charges with the magnitude less than the one trapped are being captured in circles which covers dark shade. While circles covered with the bright phase show the lowest bumps which are invisible or undetected before –5 V.

The amount of the total trapped charges is quantified in the white line circles. Using equation 8, the q'_{trap} is estimated by obtaining averaged phase profile of the set of white line circles positioned at the centre of Fig. 5 (a–c). The phase difference between ± 5 V is about 0.94 as depicted and observed from Fig. 6 (a and b). In contrast to the white circled regions where charge density and response of the different voltage bias is higher than the surroundings offered that level of energy for the positive charges is much deeper and their origin is not entirely amphoteric. However electrons can be easily trapped or detrapped in the rest of the region. Further, in BDFO/ZnO more electrons may be captured during the blocking of hole injection. As a result, due to simplicity of the modeling and the EFM Noise make it difficult to locate pinpoint the precise depths of the trapped charge. However it is observed that

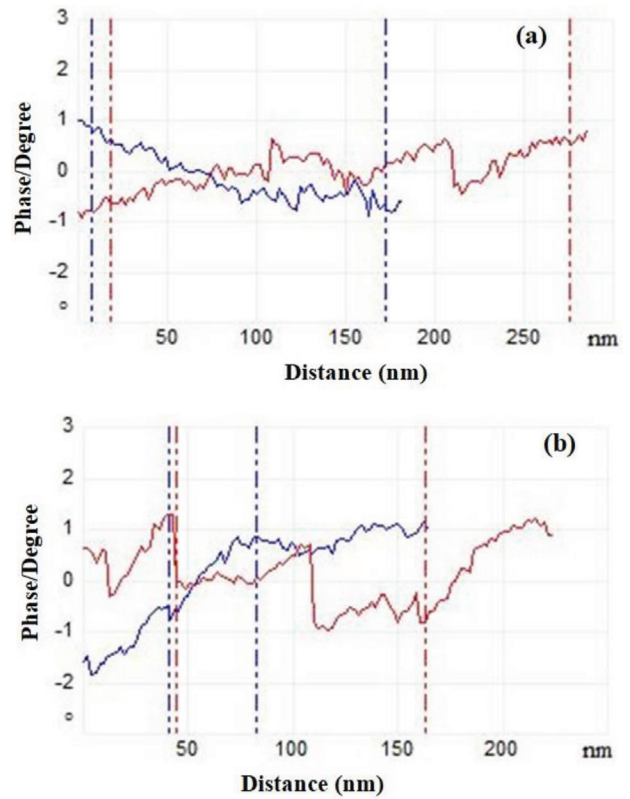


Figure 6. (a) EFM maps are of the phase shift (Distance v/s Phase) graph for Bias voltage 5V (b) Distance v/s Phase graph for Bias voltage –5V.

irregularities in the distribution of both the traps may be visualized with EFM results.

The shift in phases is measured by EFM-phase images and is obtained at different voltage biases between the Au/ZnO/Si film and the conducting probes. A plot of phase shifts within the bias range ± 5 V at a fixed lift height of 30 nm is shown in Fig. 7. The data acquired over a 500 nm scan line is averaged along the scan line and the initial trace of 0 V bias is subtracted from the obtained data. The thick solid curve is a parabolic fit to the data, employing the equation

$$y = A + Bx + Cx^2.$$

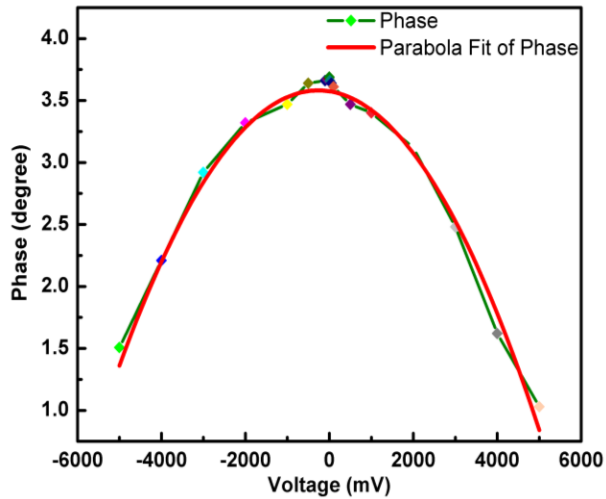


Figure 7. Phase (in degree) v/s voltage (in mV) curve.

Where, A (V) is the bias voltage in mV, B (ϕ) is the phase in degree and C is independent variable and phase difference ($\Delta\phi$) is given by equation (5).

As described by equation (5) and observed in Fig. 7, the relationship of parabolic fit phase and potential is valid for low biases only [35–37]. Due to the increased

electrostatic interactions this may not be accurate for higher voltage biases. For a particular tip the value of k_e and Q is essentially constant [38]. If the separation between the tip and the sample is maintained fixed and both the EFM tip and sample surface are metallic, d^2C/ds^2 is also constant. d^2C/ds^2 varies with the bias V , when the any of them is semiconductor (n -ZnO) as discussed above. Initially, it is assumed that d^2C/ds^2 in equation (5) does not vary with bias. The obtained data in the range of -5 to $+5$ V is fitted utilizing a parabolic method to obtain the solid curve. It can be observed from the phase shift versus voltage plot that some shaped peaks outside the parabolic function. These are found due to the change in surface potential with charge distribution. The positions of these peaks are shifted slightly while changing in the direction of voltage from (-5 V to 5 V or 5 V to -5 V).

The sets of AFM images of BDFO/ZnO thin films on 50 nm color scale and EFM images on 5° color scale are shown in Fig. 8 (a–f). The same sample scan area (500 nm) and tip lift off height is (30 nm) is selected. The sample biases are 0 V, $+5$ V and -5 V respectively. It can be seen from Fig. 8 (a–c) and (d–f) that there is no such contrast observed/discovered in case of BDFO/ZnO

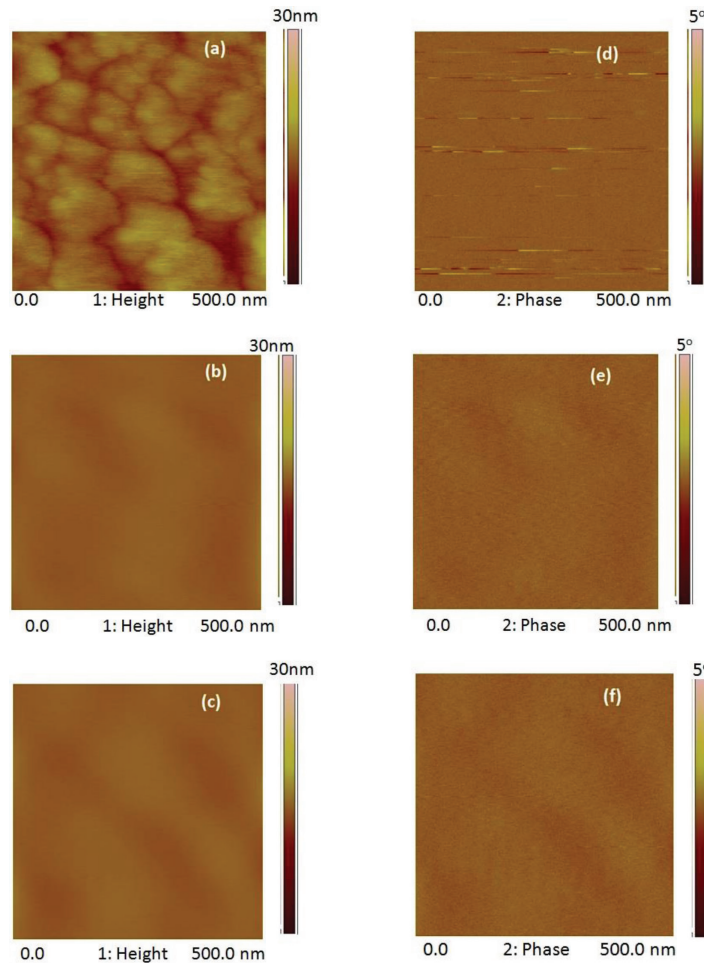


Figure 8. The sets of AFM images (a–c) of BDFO/ZnO thin films on 50 nm color scale and EFM images (d–f) on 5° color scale. Sample scan area is 500 nm and tip lift off height is 30 nm. The sample biases are 0 V, $+5$ V and -5 V respectively.

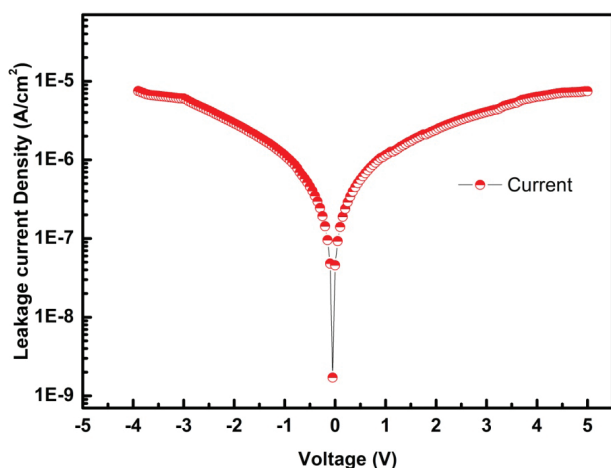


Figure 9. Leakage current density-voltage curve of BDFO/ZnO thin films.

films. Even with the application of the field the protruded space in topography images appears with almost same contrast in phase however voltage polarity is changed [in Fig. 8 (b and c)]. In the EFM images of BDFO/ZnO, contrast still remains against the voltage switching and that implies the trap sites are mainly available for electron. This may be due to good dielectric properties of BDFO. The contrast is changed only due to the presence of the capacitive forces and even if the bias is switched from +5 V to –5 V, contrast is unaltered. This bias independency ensures about the interaction between EFM tip and BDFO/ZnO stems from the image charges. The leakage current density shown in the Fig. 9 is measured of the order of 10^{-6} .

The effect of positive charges on total conductance is verified by Conductive AFM (c-AFM) with 8 V for ZnO films will be reported in another article. It is anticipated such an embedded hole in ZnO to increase the amount of total current with bias voltage by lowering the practical tunnelling barrier [39]. Thus, we can assume that protrusions observed in EFM having positive charge. These positively charged protrusions may allow electrons to easily channelled through the insulating barrier. Although very small (negligible) current spots are found in BDFO/ZnO and the increment in current is ~ 13.4 pA over the various protrusions of ZnO confirms about the occurrence of trapping of holes in the protrusions.

References

1. Mandal M., Chatterjee S., Palkar V.R Multifunctional behavior of ZnO supported $\text{Bi}_{1-x}\text{Dy}_x\text{FeO}_3$ nanorods. *J. Appl. Phys.* 2011; 110: 054313. <https://doi.org/10.1063/1.3636274>
2. Kim Y.H., Kim J.S., Kim W.M., Seong T.-Y., Lee J., Müller-Meskamp L., Leo K. Realizing the potential of ZnO with alternative non-metallic Co-dopants as electrode materials for small molecule optoelectronic devices. *Adv. Funct. Mater.* 2013; 23(29): 3645–3652. <https://doi.org/10.1002/adfm.201202799>
3. Dodds J.S., Meyers F.N., Loh K.J. Piezoelectric characterization of PVDF-TrFE thin films enhanced with ZnO nanoparticles. *IEEE Sens. J.* 2012; 12(6): 1889–1890. <https://doi.org/10.1109/JSEN.2011.2182043>

4. Conclusion

The charge trapping phenomena in the *n*-ZnO and BDFO/ZnO films were observed microscopically. It was concluded that in BDFO/ZnO, the contrast of EFM images remains constant with the bias switching and that indicates the trap sites are primarily available to host electrons. The change in contrast over the protrusions of ZnO shows that injected holes are heavily accumulated and easy mechanism of mobility of the electrical charge carriers may be through the grain boundary. The formation of these hole-trapped sites may be assumed bond breaking phenomenon. These trapped holes decrease the height of potential barrier, resulting in flow of additional amount of current. The process of EFM-phase measurements yields significant information contents about the surface of a sample. There is a possibility to excerpt the surface potential of sample, work function, capacitance and even comparison of the surface resistivity with appreciable resolution from the analysed phase data. The phase–voltage relationship was performed on a ZnO sample surface by fitting the obtained EFM-phase data using a parabolic method in the potential range of –5 to +5 V. Thus phase data may be converted to voltage data, and enables the use of EFM phase mode for measuring the surface potential of an unknown region. The validity of this procedure is both for semiconductor and metallic surfaces. Finally, a good understanding has been found about the electrical charge transport on ZnO and BDFO/ZnO thin films from these results. It may provide its relevant improvements for application as a piezoelectric layer and memory element in MEMS energy scavengers, transparent electrodes in some photovoltaic devices and on chip transformers.

Acknowledgement

The authors wish to acknowledge the partial funding (Grant No. 08DIT006 and 13DIT006) received from the Department of Information Technology, Government of India, through the Centre of Excellence in Nanoelectronics, IIT Bombay under INUP. The authors also acknowledge to Department of Physics and Department of Material Science, IIT Bombay and Rajasthan Technical University, Kota for experimental help.

4. Prepelita P., Medianu R., Garoi F., Stefan N., Iacomì F. On the structural and electrical characteristics of zinc oxide thin films. *Thin Solid Films*. 2010; 518(16): 4615–4618. <https://doi.org/10.1016/j.tsf.2009.12.044>
5. de la L Olvera M., Maldonado A., Asomoza R., Tirado-Guerra S. Characteristics of transparent and conductive undoped ZnO thin films obtained by chemical spray using zinc pentanedionate. *Thin Solid Films*. 2002; 411(2): 198–202. [https://doi.org/10.1016/S0040-6090\(02\)00248-1](https://doi.org/10.1016/S0040-6090(02)00248-1)
6. Pearton S.J., Norton D.P., Heo Y.W., Tien L.C., Ivill M.P., Li Y., Kang B.S., Ren F., Kelly J., Hebard A.F. ZnO spintronics and nanowire devices. *J. Electron. Mater.* 2006; 35(5): 862–868. <https://doi.org/10.1007/BF02692541>
7. Nagata T., Oh S., Yamashita Y., Yoshikawa H., Ikeno N., Kobayashi K., Chikyow T., Wakayama Y. Photoelectron spectroscopic study of band alignment of polymer/ZnO photovoltaic device structure. *Appl. Phys. Lett.* 2013; 102(4): 043302–043304. <https://doi.org/10.1063/1.4790298>
8. Maragliano C., Stefancich M., Rampino S., Colace L. Realistic simulation of polycrystalline CIGS absorbers and experimental verification. *MRS Online Proceedings Library*. 2013; 1493: 153–160. <https://doi.org/10.1557/opl.2013.401>
9. Repins I., Contreras M., Romero M., Yan Y., Metzger W., Li J., Johnston S., Egaas B., DeHart C., Scharf J., McCandless B.E., Noufi R. Characterization of 19.9%-efficient CIGS absorbers. *33rd IEEE Photovoltaic Specialists Conference*. 2008; 235–239. <https://doi.org/10.1109/PVSC.2008.4922628>
10. Maragliano C., Colace L., Chiesa M., Rampino S., Stefancich M. Three-dimensional $\text{Cu}(\text{InGa})\text{Se}_2$ photovoltaic cells simulations: optimization for limited-range wavelength applications. *IEEE J. Photovoltaics*. 2013; 3(3): 1106–1112. <https://doi.org/10.1109/JPHOTOV.2013.2258191>
11. Lilliu S., Agostinelli T., Pires E., Hampton M., Nelson J., Macdonald J.E. Dynamics of crystallization and disorder during annealing of P3HT/PCBM bulk heterojunctions. *Macromolecules*. 2011; 44(8): 2725–2734. <https://doi.org/10.1021/ma102817z>
12. Krebs F.C. Fabrication and processing of polymer solar cells: A review of printing and coating techniques. *Sol. Energy Mater. Sol. Cells*. 2009; 93(4): 394–412. <https://doi.org/10.1016/j.solmat.2008.10.004>
13. Scott J.F. Data storage: Multiferroic memories. *Nat. Mater.* 2007; 6: 256–257. <https://doi.org/10.1038/nmat1868>
14. He C., Ma Z.-J., Sun B.Z., Sa R.J., Wu K. The electronic, optical and ferroelectric properties of BiFeO_3 during polarization reversal: A first principle study. *J. Alloy Comp.* 2015; 623: 393–400. <https://doi.org/10.1016/j.jallcom.2014.11.062>
15. Peng Lin, Simin Cui, Xierong Zeng, Haitao Huang, Shanming Ke. Giant dielectric response and enhanced thermal stability of multiferroic BiFeO_3 . *J. Alloy Comp.* 2014; 600: 118–124. <https://doi.org/10.1016/j.jallcom.2014.02.128>
16. Sunil Chauhan, Manoj Kumar, Sandeep Chhoker, Katyaj S.C. A comparative study on structural, vibrational, dielectric and magnetic properties of microcrystalline BiFeO_3 , nanocrystalline BiFeO_3 and core-shell structured $\text{BiFeO}_3@SiO_2$ nanoparticles. *J. Alloy Comp.* 2016; 666: 454–467. <https://doi.org/10.1016/j.jallcom.2016.01.116>
17. Chia-Shiu Yeh, Jenn-Ming Wu. Characterization of Pt/multiferroic $\text{BiFeO}_3/(\text{Ba,Sr})\text{TiO}_3/\text{Si}$ stacks for nonvolatile memory applications. *Appl. Phys. Lett.* 2008; 93(15): 154101. <https://doi.org/10.1063/1.3001800>
18. Palkar V.R., Prashanthi K. Observation of magnetoelectric coupling in $\text{Bi}_{0.7}\text{Dy}_{0.3}\text{FeO}_3$ thin films at room temperature. *Appl. Phys. Lett.* 2008; 93(13): 132906. <https://doi.org/10.1063/1.2994692>
19. Prashanthi K., Chalke B.A., Bapat R.D., Purandare S.C., Palkar V.R. Multiferroic $\text{Bi}_{0.7}\text{Dy}_{0.3}\text{FeO}_3$ thin films directly integrated on Si for integrated circuit compatible devices. *Thin Solid Films*. 2010; 518(20): 5866–5870. <https://doi.org/10.1016/j.tsf.2010.05.060>
20. Fain (Jr.) S.C., Barry K.A., Bush M.G., Pittenger B., Louie R.N. Measuring average tip-sample forces in intermittent-contact (tapping) force microscopy in air. *Appl. Phys. Lett.* 2000; 76(7): 930–932. <https://doi.org/10.1063/1.125633>
21. Lei C.H., Das A., Elliott M., Macdonald J.E. Quantitative electrostatic force microscopy-phase measurements. *Nanotechnology*. 2004; 15(5): 627–634. <https://doi.org/10.1088/0957-4484/15/5/038>
22. Sarid D. Scanning force microscopy: with applications to electric. Magnetic and Atomic Forces. Oxford: Oxford University, 1994.
23. Bonnell D. Scanning probe microscopy and spectroscopy: theory, techniques and applications. New York: Wiley-VCH, 2000.
24. Serry F.M., Kjoller K., Thornton J.T., Tench R.J., Cook D. Electric force microscopy surface potential imaging and surface electric modifications with AFM. Bruker, 2010. URL: <http://nano.boisestate.edu/wp-content/uploads/2010/12/Bruker-AN-27-EFM-Surface-Potential.pdf>
25. Kim J.-H., Noh H., Khim Z.G., Jeon K.S., Park Y.J., Yoo H., Choi E., Om J. Electrostatic force microscopy study about the hole trap in thin nitride/oxide/semiconductor structure. *Appl. Phys. Lett.* 2008; 92(13): 132901. <https://doi.org/10.1063/1.2904646>
26. Kang C.J., Buh G.H., Lee S., Kim C.K., Mang K.M., Im C., Kuk Y. Charge trap dynamics in a SiO_2 layer on Si by scanning capacitance microscopy. *Appl. Phys. Lett.* 1999; 74(13): 1815. <https://doi.org/10.1063/1.123095>
27. Wangsness R.K. Electromagnetic field. New York: Wiley, 1979.
28. Majumdar S., Banerji P. Temperature dependent electrical transport in $p\text{-ZnO}/n\text{-Si}$ heterojunction formed by pulsed laser deposition. *J. Appl. Phys.* 2009; 105(4): 043704. <https://doi.org/10.1063/1.3078806>
29. Bhatia D., Roy S., Nawaz S., Meena R.S., Palkar V.R. Room temperature electrical properties of $\text{Bi}_{0.7}\text{Dy}_{0.3}\text{FeO}_3$ thin films deposited by PLD on ZnO films for potential applications. *Microelectronic Engineering*. 2016; 163: 60–66. <https://doi.org/10.1016/j.mee.2016.06.003>
30. Somvanshi D., Jit S. Analysis of temperature-dependent electrical characteristics of $n\text{-ZnO}$ nanowires (NWs)/ $p\text{-Si}$ heterojunction diodes. *IEEE Transactions on Nanotechnology*. 2014; 13(1): 62–69. <https://doi.org/10.1109/TNANO.2013.2290553>
31. Lee J.D., Park C.Y., Kim H.S., Lee J.J., Choo Y.G. A study of conduction of ZnO film/ $p\text{-Si}$ heterojunction fabricated by photo induced electro deposition under illumination. *J. Phys. D: Appl. Phys.* 2010; 43(36): 365403-1–365403-6. <https://doi.org/10.1088/0022-3727/43/36/365403>
32. Qian F.Z., Jiang J.S., Guo S.Z., Jiang D.M., Zhang W.G. Multiferroic properties of $\text{Bi}_{1-x}\text{Dy}_x\text{FeO}_3$ nanoparticles. *J. Appl. Phys.* 2009; 106(8): 084312. <https://doi.org/10.1063/1.3245390>
33. Tao Xu, Guoying Wu, Guobing Zhang, Yilong Hao. The compatibility of ZnO film with micromachining process. *Sensors and Actuators A: Physical*. 2003; 104(1): 61–67. [https://doi.org/10.1016/S0924-4247\(02\)00484-3](https://doi.org/10.1016/S0924-4247(02)00484-3)
34. Yao Wang, Ce-Wen Nan. Integration of BiFeO_3 thin films on Si wafer via a simple sol-gel method. *Thin Solid Films*. 2009; 517(15): 4484–4487. <https://doi.org/10.1016/j.tsf.2009.02.142>

35. Middleton A.A., Wingreen N.S. Collective transport in arrays of small metallic dots. *Phys. Rev. Lett.* 1993; 71(19): 3198. <https://doi.org/10.1103/PhysRevLett.71.3198>
36. Bresse J.-F. Contact potential difference of Au and GaInAs by electrostatic force microscopy. *Microchimica Acta.* 2000; 132(2–4): 449–455. <https://doi.org/10.1007/s006040050093>
37. Sze S.M. Physics of semiconductor devices. Chichester: Wiley, 1981.
38. Rousier R., Vairac P., Cretin B. Measurement of the contact potential difference with an electrostatic force microscope. *Eur. J. Phys.* 2001; 22(6): 657–662. <https://doi.org/10.1088/0143-0807/22/6/311>
39. Seko A., Watanabe Y., Kondo H., Sakai A., Zaima S., Yasuda Y. Analysis of local breakdown process in stressed gate SiO₂ films by conductive atomic force microscopy. *Jpn. J. Appl. Phys.* 2005; 10(44 Pt 1): 7582–7587. <https://doi.org/10.1143/JJAP.44.7582>